

# From Fog Chamber to Aircraft Window: Pixel-Registered Imaging and Synthetic Fine-Tuning Enable Cross-Domain Defogging

ALEXANDER INGOLD,<sup>1</sup> SABINA D. MENON,<sup>2</sup> MANYA YELLEPEDDY,<sup>2</sup>  
ALEC IKEI,<sup>2</sup> JOHN D. HODGES,<sup>2</sup> JORDAN BAKER,<sup>2</sup> SYED N. QADRI,<sup>2</sup>  
AND RAJESH MENON<sup>1,\*</sup>

<sup>1</sup> Department of Electrical and Computer Engineering, University of Utah, Salt Lake City, UT 84112, USA

<sup>2</sup> U.S. Naval Research Laboratory Remote Sensing Division, Washington DC 20375, USA.

\*rmenon@eng.utah.edu

**Abstract:** A deep defogging pipeline pretrained on controlled laboratory fog and fine-tuned with domain-randomized synthetic fog applied to clear outdoor scenes generalizes across a graded sequence of out-of-distribution settings with no target-domain training, from chamber-free free-flowing fog to iPhone video recorded through an aircraft cabin window in flight, an entirely unseen sensor, scene, and optical path. This directly addresses an open transfer limitation reported for real-world binocular defogging. Two design choices support the transfer. First, a single-camera fog imager photographs a flat-panel display through an artificial-fog enclosure with a fixed 114 mm scattering path, producing 5,495 pixel-aligned foggy/clear pairs. Exact registration permits a paired Laplacian ratio that predicts per-image restoration quality far better than single-image proxies (Spearman  $\rho = 0.632$  versus 0.399) and supports pixel-exact  $L_1$  reconstruction training that avoids adversarial hallucination. Second, the fog-chamber checkpoint is fine-tuned on Mapillary Vistas crops overlaid with on-the-fly randomized synthetic fog spanning a broad range of strengths, spatial variations, airlights, and noise conditions. On a 552-image held-out split, a uniform comparison of 30 restoration backbones places NAFNet at the top (24.33 dB / 0.7912 SSIM), with a compact alternative within 1.29 dB at 3% of the parameter count, and a ResNet-50 classifier confirms that the restoration preserves semantic content rather than only pixel-level structure. On unpaired aircraft-window video, NIQE decreases from a mean of 6.22 to 4.97 after fine-tuning, with temporally stable output across full-motion sequences. The same backbone, under paired supervision, also reaches 20.71 dB / 0.683 SSIM on a non-overlapping O-HAZE/NH-HAZE split (a transferability check rather than a competitive ranking).

## 1. Introduction

Fog and haze attenuate scene radiance along the line of sight and add scattered ambient light, reducing contrast and suppressing fine detail. The standard atmospheric scattering model expresses an observed pixel as a convex mixture of the attenuated scene radiance and the airlight, weighted by a transmission term that decays with optical depth [1, 2]. Recovering a clear image from a single foggy observation is therefore underconstrained: scene radiance, airlight, and depth-dependent transmission are all unknown from one measurement per pixel [2].

### 1.1. Prior-based and learned restoration

Early methods made the inverse problem tractable with statistical priors on outdoor scenes, notably the dark channel prior [3] and the color attenuation prior [4]. These priors are interpretable but fail for bright or white content, unusual materials, and dense or spatially uniform fog, and have no mechanism for non-natural capture geometries. Deep learning shifted the field toward learned restoration: DehazeNet [5] and AOD-Net [6] estimated or embedded the scattering model; GridDehazeNet [7], FFA-Net [8], and DehazeFormer [9] added multi-scale and attention mechanisms; and general-purpose backbones such as NAFNet [10] showed that streamlined

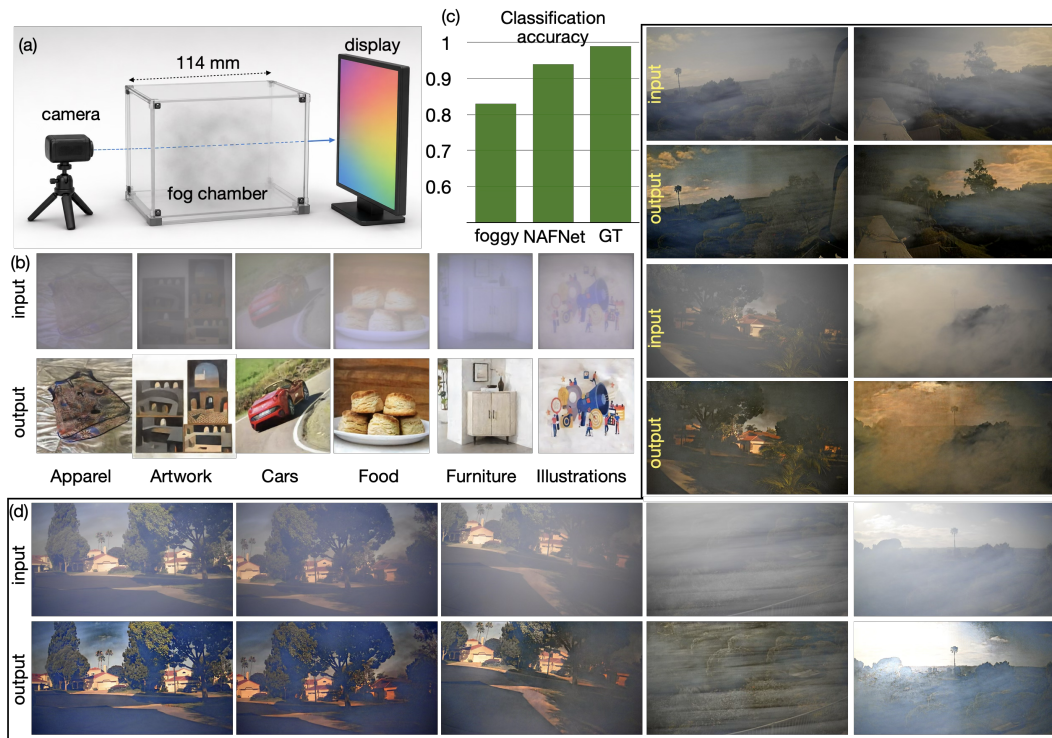


Fig. 1. Controlled fog-chamber training, benchmark results, and generalization to chamber-free fog. (a) Pipeline overview: foggy images are captured through a fog chamber with a fixed 114 mm scattering path, and the pixel-registered ground-truth images are used to train a deep restoration network with pixel-exact  $L_1$  supervision. (b) Representative test-set results across the six content categories (top row: foggy input; bottom row: NAFNet prediction); on the 552-image held-out split NAFNet attains mean PSNR / SSIM of 24.33 dB / 0.7912. (c) Category-classification accuracy of a ResNet-50 evaluated on foggy inputs, NAFNet-defogged outputs, and ground-truth images, quantifying how much semantic content the restoration recovers relative to fog degradation. (d) Transfer to chamber-free fog generated by the fog machine placed directly in front of the camera, producing spatially nonuniform, time-varying scattering across a range of outdoor scenes (top row: foggy input; bottom row: defogged output). Together, panels (b)–(d) show that the trained model restores both pixel-level structure and semantic content under controlled fog and continues to remove the bulk of the scattering when the fog dynamics depart from the chamber regime.

direct-reconstruction networks rival more complex designs. Surveys nevertheless emphasize a persistent gap between synthetic-benchmark and real-haze performance [11], and no large, uniformly trained benchmark of modern backbones exists for an optically controlled, exactly paired fog dataset.

### 1.2. Real-world paired data and the transfer problem

Because aligned foggy/clear pairs are hard to acquire outdoors, the field has relied on synthetic data, from SYNTHIA [12] and Foggy Cityscapes [13] to curriculum adaptation [14]. A central limitation is synthetic training can fail when the generated fog distribution is too narrow or does not match real imaging conditions, and unpaired adversarial translation [15, 16] introduces hallucination risk when faithful reconstruction matters. Real paired benchmarks such as O-HAZE [17] and NH-HAZE [18] anchor the NTIRE challenges [19, 20] but contain only tens of scenes, and recent methods continue to push real-image dehazing [21, 22].

Most directly relevant to the present work, Pollak and Menon introduced Stereofog, a 10,067-pair real-world binocular dataset, and demonstrated effective  $\text{pix} \times 2 \text{pix}$  defogging even under dense fog [23]. That study reached two conclusions that motivate this paper. First, models trained on generic synthetic fog failed on real images. Second, and more fundamentally, the learned models transferred poorly to different cameras and scenes without retraining, which the authors attributed to adaptation to specific recording hardware. The binocular design also captures the two views with separate cameras, introducing residual misregistration that required shift-robust metrics and favored adversarial translation, whose hallucination tendency the authors flagged as a limitation. Whether a controlled, exactly registered capture system combined with randomized synthetic fog fine tuning can instead produce models that transfer across hardware and scenes has remained open.

### 1.3. Gaps and contributions

The prior literature leaves four gaps: no optically controlled, exactly paired fog dataset large enough for a uniform many-model benchmark; little use of paired data to characterize the fog itself and cross-domain generalization almost never tested from a controlled imager to a completely different consumer sensor and scene, let alone to motion video. We address these with an end-to-end study centered on data, a paired difficulty metric, and a domain-randomized synthetic pipeline; we deliberately use existing restoration backbones rather than introducing a new architecture, so improvements isolate to the data and training regime. Our contributions are:

1. **Cross-domain transfer across a graded out-of-distribution sequence, including aircraft-window iPhone video.** A model trained only on controlled fog-chamber pairs and domain-randomized synthetic outdoor fog defogs (i) chamber-free free-flowing fog generated by a fog machine placed in front of the camera, in which the optical depth along the line of sight is no longer fixed by a geometry (Fig. 1d), and (ii) iPhone video captured through an aircraft cabin window in flight, with no target-domain training and temporally stable output across full-motion sequences (Fig. 2; Visualizations 1 and 2). This directly addresses the cross-hardware transfer limitation reported for real-world binocular defogging [23].
2. **A controlled, exactly registered fog imager and a 5,495-pair dataset.** A display-based imager photographs a flat-panel display through an artificial-fog enclosure with a fixed 114 mm scattering path. Unlike binocular capture [23], single-camera display imaging gives exact pixel registration, which both removes the need for shift-robust metrics and enables direct reconstruction training that avoids adversarial hallucination.
3. **A paired fog-difficulty metric.** The mean-absolute Laplacian ratio, a paired refinement of the single-image Laplacian variance used to grade fog density in prior work [23], predicts

per-image restoration quality with Spearman  $\rho = 0.632$  (category-centered 0.590), far exceeding the best single-image proxy ( $\rho = 0.399$ ).

4. **A 30-model benchmark with a semantic-content check.** Thirty restoration backbones are trained under identical conditions on the fog-chamber dataset, establishing a reproducible baseline across contemporary defogging architectures and generic image-to-image models. NAFNet [10] ranks highest (24.33 dB / 0.7912 SSIM), while SpecAT S2 [24] is within 1.29 dB at 3% of the parameter count. A ResNet-50 classifier evaluated on foggy, defogged, and clear inputs shows that classification is already feasible directly from foggy images, and that NAFNet defogging closes most of the residual gap to ground truth (Fig. 1c), confirming that the restoration preserves semantic content rather than only low-level appearance.
5. **Domain-randomized synthetic fine-tuning and task-specific checks.** The fog-chamber NAFNet checkpoint is fine-tuned on Mapillary Vistas clear crops with on-the-fly spatial synthetic fog. Light-fog measurements set only loose generator ranges; the final transfer model uses randomized fog strength, airlight, spatial variation, contrast, color, and noise rather than optimization to a narrow unpaired reference set. The same backbone is also evaluated under paired task-specific fine-tuning on O-HAZE, NH-HAZE, and the NTIRE 2026 nighttime probe.

The dataset, code, simulator, trained models, and demonstration videos are released publicly with the reproducibility package. Section 2 describes the chamber geometry and paired metric, Section 3 the methods, Section 4 the results, Section 5 the discussion, and Section 6 concludes. The supplement provides split audits, metric definitions, the full benchmark table, classification and dark-channel-prior checks, simulator details, public real-haze protocols, fog-density statistics, and paired structure-loss analysis.

## 2. Chamber geometry and Paired Metric

### 2.1. Scattering model background and chamber geometry

The atmospheric scattering model [2] writes the observed pixel as

$$\mathbf{I}(\mathbf{x}) = \mathbf{J}(\mathbf{x})T(\mathbf{x}) + \mathbf{A}[1 - T(\mathbf{x})], \quad T(\mathbf{x}) = e^{-\beta d(\mathbf{x})}, \quad (1)$$

where  $\mathbf{J}$  is the clear radiance,  $\mathbf{A}$  the global airlight,  $T$  the transmission,  $\beta$  the extinction coefficient, and  $d$  the path length. For the fog imager  $d$  is fixed by the chamber geometry. We use this model as a physical motivation for the synthetic fog simulator, not as a radiometric inversion of the fog-chamber data. The display, camera response, exposure and fog radiance were not independently calibrated, so we do not estimate a physical transmission map or extinction coefficient from the image pairs. The acrylic fog chamber had a 114 mm fog path-length and  $133 \times 114$  mm transverse dimensions (see Fig. 1). Artificial fog was generated by an Eliminator Lighting VF400-E theatrical fog machine using propylene-glycol fluid.

### 2.2. A paired fog-difficulty metric

Prior real-world work graded image-level fog severity by the variance of the Laplacian of the foggy image alone [23]. Exact registration lets us instead form a *paired* high-frequency retention ratio,

$$R_{\nabla^2} = \frac{\text{mean}(|\nabla^2 \mathbf{I}_{\text{fog}}|)}{\text{mean}(|\nabla^2 \mathbf{I}_{\text{clear}}|)}, \quad (2)$$

which measures how much of the clear image’s local high-frequency structure survives the fog and normalizes out scene content. On the 552-image split,  $R_{\nabla^2}$  at one-pixel scale predicts per-image

NAFNet PSNR with Spearman  $\rho = 0.632$  (category-centered 0.590), substantially better than the best single-image proxy (dark-channel 90th percentile,  $\rho = 0.399$ ; category-centered 0.312). Supplementary Fig. S7 summarizes the metric ranking, per-image relationship to NAFNet PSNR, and a representative paired Laplacian example. The full-metric search is in Supplement section S10 and the image-domain power-spectral-density (PSD) analysis is in Supplement section S9. The PSD analysis shows that high-frequency power retention was 8.9 $\times$  lower than low-frequency retention in paired fog/clear images.

### 3. Methods

#### 3.1. Apparatus and dataset

As illustrated in Fig. 1(b), a flat-panel LCD presents the ground-truth target through an acrylic enclosure of internal path length 114 mm and transverse cross-section 133  $\times$  114 mm, with fog from the VF400-E machine; in some runs a vertical linear polarizer was placed before the camera (noted where used). Single-camera display imaging yields exact pixel registration without post-hoc alignment, in contrast to binocular capture [23], and lets us train with pixel-exact  $L_1$  reconstruction rather than adversarial losses (Fig. 1a). Ground-truth images are drawn from a public 130k-image archive at 512  $\times$  512 across six categories [25]. A deterministic every-tenth split yields 4,943 training and 552 held-out pairs (92 per category; 5,495 total). Full dataset roles and split audits are in Supplement section S1.

#### 3.2. Benchmark, classification, simulator, and adaptation

We trained thirty restoration backbones on the fog-chamber training split under identical conditions: pixel-exact  $L_1$  loss, Adam optimizer [26], learning rate  $10^{-4}$ , 50 epochs, and 512  $\times$  512 inputs (memory-heavy models used crops at the same resolution). Each model was evaluated on the 552-image held-out split by mean MAE, MSE, PSNR, and SSIM [27], with LPIPS [28] additionally reported for the top five. NAFNet [10] ranked highest and was used as the backbone for every downstream fine-tuning stage in this paper except for the ablation run with random weight initialization.

To assess whether restoration preserves semantic content rather than merely pixel-level structure, we trained a ResNet-50 classifier [29] on five dataset categories excluding illustrations and evaluated it on clear, foggy, and NAFNet-defogged images (Fig. 1c). Classification from foggy inputs already retains most of the ground-truth accuracy, and NAFNet-defogged inputs close most of the remaining gap, indicating that the restoration recovers semantically discriminative content rather than only low-level appearance.

To bridge from chamber fog to outdoor fog, the fog-chamber NAFNet checkpoint was fine-tuned on clear Mapillary Vistas crops [30] with on-the-fly spatial synthetic fog (Supplement section S6). The split contained 18,000 training, 2,000 validation, and 5,000 test clear images. Training used 512  $\times$  512 crops, AdamW [31], cosine learning-rate decay from  $10^{-4}$  to 0, and one epoch capped at 2,600 training batches. Each crop sampled fog strength, spatial variation, airlight color, contrast, saturation, edge veil, blur, and noise. Free-space light-fog image statistics were used only to choose plausible initial ranges for these random variables, not to fit a fixed generator and not as training, validation, or test images. Synthetic validation and test PSNR were 21.38 dB and 21.17 dB, respectively, and are treated only as synthetic-training diagnostics. The matched no-pretraining ablation reached 16.47 dB validation and 16.58 dB test PSNR under the same synthetic recipe.

For paired real-haze adaptation, the fog-chamber NAFNet was fine-tuned with paired supervision on a non-overlapping mixed split of O-HAZE [17] and NH-HAZE [18]. We additionally report a two-image internal-test probe of the NTIRE 2026 nighttime dehazing challenge [32, 33] as a sanity check of paired adaptation under nighttime conditions; no challenge rank is claimed.

Splits, hyperparameters, and per-image metrics are detailed in the Supplement.

Complete protocols for the benchmark, randomized synthetic fine-tuning, public paired-haze checks, NTIRE probe, fog statistics, PSD analysis, and paired structure-loss analysis are detailed in Supplement sections S3–S10.

### 3.3. *Out-of-distribution evaluation*

We applied the synthetic fine-tuned model, with no target-domain training, to two evaluations that progressively stress its generalization: outdoor captures with a fog machine placed directly in front of the camera (no enclosure), and video from a consumer iPhone (iPhone 13, iOS 26.5) recorded through an aircraft passenger-cabin window in daylight and at dusk.

The chamber-free fog captures probe transfer to spatially nonuniform, time-varying scattering, in which the optical depth along the line of sight is no longer fixed by a geometry as it is in the chamber. Representative frames are shown in Fig. 1d; the model removes the bulk of the scattering while preserving scene structure, indicating that the learned restoration is not tied to the chamber’s fixed 114 mm path length.

The aircraft-window evaluation is the strongest transfer test in the paper. Four factors make it out of distribution simultaneously. First, the cabin glass introduces scattering and specular reflections that are absent from training. Second, the aerial scene content (sky, clouds, terrain at oblique view) is unlike any image in the training set. Third, the iPhone sensor and its on-device tone mapping differ from the chamber camera. Fourth, video demands frame-to-frame temporal consistency that single-frame training never supervised. With no aligned references we cannot report PSNR/SSIM; instead we report the no-reference Natural Image Quality Evaluator (NIQE) [34], for which lower values indicate higher perceived quality, together with the demonstration videos (Visualizations 1 and 2). Representative frames are shown in Fig. 2 with the per-frame NIQE value overlaid on each panel.

## 4. Results

### 4.1. *Zero-shot transfer to aircraft-window video*

The pipeline’s central result is cross-domain transfer with no target-domain training. Fine-tuning the fog-chamber NAFNet on synthetic outdoor fog reached 21.17 dB on a held-out split of the same synthetic distribution; this number quantifies fit to the simulator, not real-fog transfer, which we evaluate below. The decisive evidence is qualitative transfer to real, unrelated fog (Fig. 2). The fog-chamber model alone over-corrects outdoor and aircraft-window inputs with color shifts and artifacts, while randomized synthetic fine-tuning removes this failure.

Applied to iPhone video through an aircraft cabin window, the pipeline produces temporally stable output across full-motion sequences without visible flicker or frame-to-frame color drift in the demonstration clips (Visualizations 1 and 2). While NIQE did not decrease for every image, NIQE decreased on average from 6.22 to 4.97 for the unpaired aircraft-window examples (Fig. 2; Supplementary Table S12). This directly answers the open question from real-world binocular defogging, where models did not generalize across cameras and scenes without retraining [23]: a controlled exactly registered capture followed by synthetic fine-tuning yields a model that does. Two demonstration videos accompany the paper and are the most direct evidence of practical utility; static metrics cannot establish temporal stability.

### 4.2. *Public paired real-haze adaptation*

The same backbone adapts under paired supervision. On a non-overlapping mixed split it reached 20.71 dB / 0.683 SSIM (O-HAZE subset 22.65 / 0.726; NH-HAZE subset 18.77 / 0.640; the 3.88 dB gap reflects non-homogeneous haze). Exemplary results are summarized in Fig. 3. These are controlled transferability checks, not competitive claims; dedicated O-HAZE methods

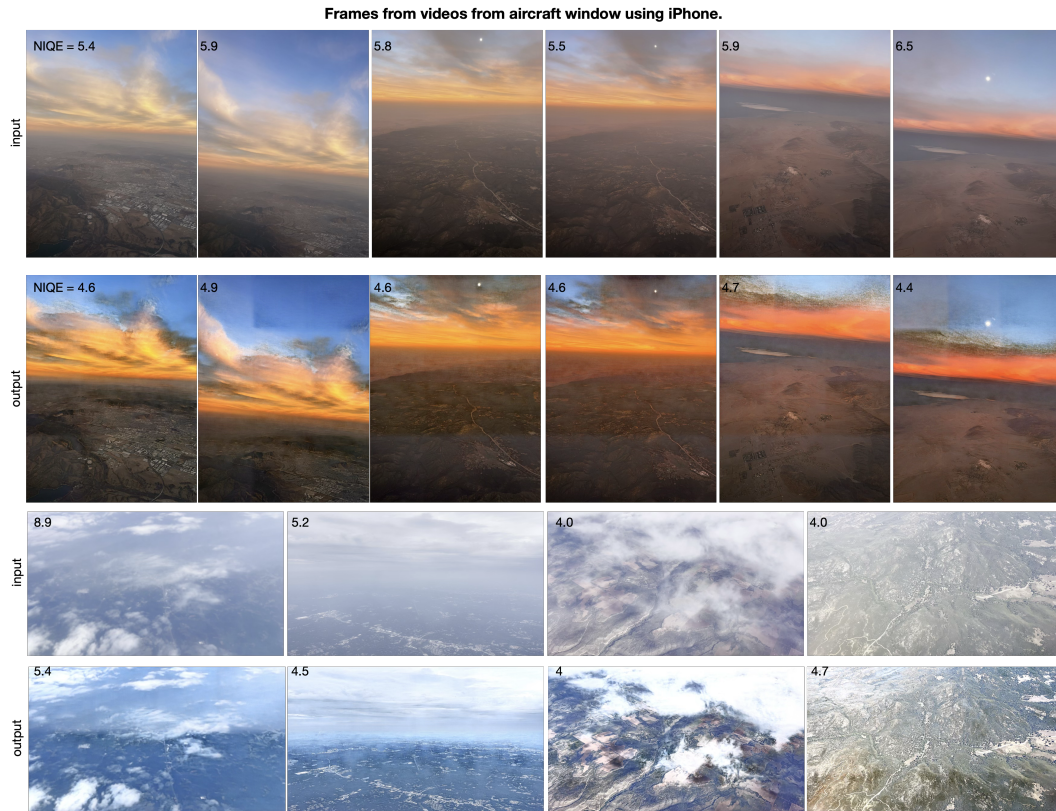


Fig. 2. Testing our trained model on videos captured using an iPhone camera through an aircraft window at high altitudes under different conditions including dusk and bright daylight. In all cases, the trained network is able to reduce visible fog, but loss of dynamic range especially at the brightest pixels are seen. This is particularly impressive since such images and camera are completely foreign to the network. Since ground-truth is not available for these images, we report the NIQE metric in each image. Also see Visualizations 1 and 2.

exceed 24 dB [21, 22]. Applying the synthetic model directly, without real-haze fine-tuning, over-corrects these inputs, showing the regimes are complementary. The discrepancy with the aircraft-window result likely reflects the absence of ground truth there: over-correction that depresses PSNR on O-HAZE/NH-HAZE may go partially undetected in a reference-free NIQE evaluation. Real-fog video with aligned references is the natural next-step measurement (see Limitations). An NTIRE 2026 nighttime probe reached 24.77 dB / 0.770 SSIM on a two-image internal split (a probe only, no challenge rank claimed) [32, 33]. Category recognizability and classification results are in Supplement S4.

#### 4.3. Benchmark and paired difficulty metric

NAFNet ranked highest on the 552-image split with mean PSNR 24.33 dB (95% bootstrap CI, 24.00–24.65) and SSIM 0.7912 (95% bootstrap CI, 0.7808–0.8012), a 12.53 dB gain over the foggy-input baseline (11.80 dB); SpecAT S2 [24] and RegGAN followed at 23.04 and 22.54 dB. The parameter-efficiency frontier (Fig. 4) has two anchors: NAFNet (29.16 M params) for accuracy and SpecAT S2 (0.99 M) for efficiency, the latter within 1.29 dB at  $\approx 3\%$  of the parameters; intermediate models are Pareto-dominated (*i.e.*, worse on both axes than at least one

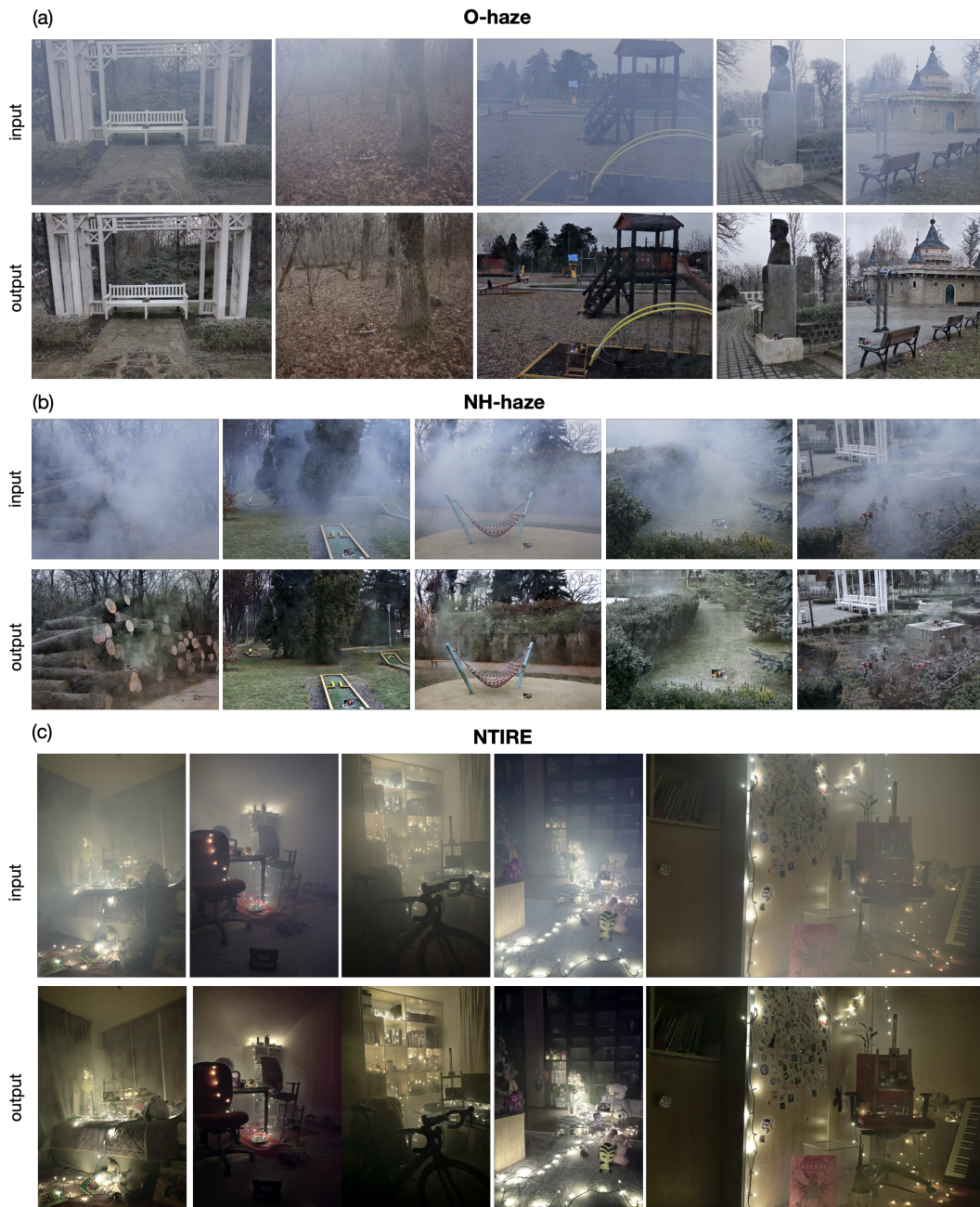


Fig. 3. Task-specific public-haze and nighttime-haze checks. (a) O-HAZE, (b) NH-HAZE and (c) NTIRE. Various exemplary images with different fog severities are successfully defogged. The previously trained models were fine-tuned to the dataset for best results. Quantitative split definitions and per-image metrics are reported in Supplement section S7

of NAFNet or SpecAT S2). Notably, `pix2pix`, the adversarial backbone used for binocular real-world defogging [15, 23], ranks low here (15.58 dB): exact registration favors direct L1 reconstruction over adversarial translation in this regime. The dark channel prior [3] reduced PSNR below the foggy input (11.80  $\rightarrow$  9.82 dB), consistent with the display back-illumination violating its outdoor assumptions. The full 30-model table is in Supplement table S2.

Per-category PSNR spans 3.42 dB (artwork 23.02, furniture 26.44). Categories with dense fine structure retain less high-frequency content at a given fog level and are harder to restore (Supplement section S10).

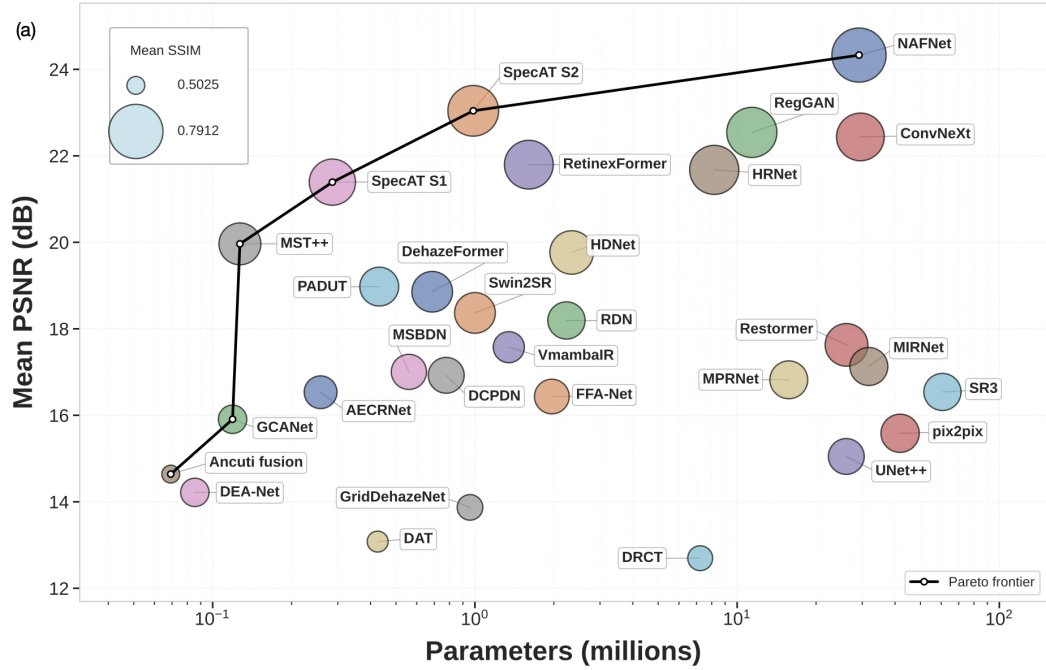


Fig. 4. Defogging benchmark across established models on the fog-chamber dataset. (a) Thirty-model benchmark summary: marker area encodes mean SSIM, the horizontal axis shows parameter count, and the vertical axis shows mean PSNR; the black line marks the Pareto frontier for higher PSNR with fewer parameters. (b) Exemplary images from left to right: input foggy, outputs from RegGAN, SpecAT S2 and NAFNet, and ground-truth.

## 5. Discussion

The results resolve a tension in prior real-world defogging. Pollak and Menon found that models trained on a large real-world paired dataset transferred poorly across cameras and scenes, and that generic synthetic fog failed on real images [23]. Two design choices in the present work recover

that transfer. First, single-camera display imaging gives exact pixel registration, which enables pixel-exact  $L_1$  reconstruction and so avoids the adversarial hallucination that the binocular setting had to tolerate; the same registration underwrites the paired Laplacian ratio of Section 3. Second, randomized synthetic fine-tuning exposes the fog-chamber model to a broad family of spatially varying outdoor-like scattering conditions. The two capture regimes are complementary points in a design space: binocular capture trades registration for real three-dimensional scene content, while display capture trades scene realism for exact registration and content control. The OE-relevant lesson is that, for a fixed scattering path and controlled illumination, a carefully posed imaging setup plus a domain-randomized forward model can substitute for outdoor data collection in a regime where outdoor collection is impractical.

The aircraft-window result and the O-HAZE/NH-HAZE result appear asymmetric and deserve direct treatment. The synthetic fine-tuned model transfers to iPhone aircraft-cabin video without target-domain training, yet the same model over-corrects O-HAZE/NH-HAZE inputs under reference-based scoring (Section 4). The most plausible reconciliation is that the aircraft evaluation is reference-free (NIQE only) and so cannot penalize over-correction the way PSNR/SSIM does on O-HAZE/NH-HAZE. We therefore frame the aircraft-window result as evidence that the pipeline produces visually coherent, temporally stable output on an entirely unseen sensor, scene, and optical path, rather than as a quantitative generalization claim. Establishing the stronger claim requires aligned cross-hardware references, which the present pipeline does not yet provide.

For practitioners, the benchmark gives two actionable findings. SpecAT S2 matches NAFNet within 1.29 dB at roughly 3% of the parameters, making it the natural choice when compute or memory is constrained, and NAFNet is the natural choice when accuracy dominates. More broadly, exact-registration training favors direct  $L_1$  reconstruction over adversarial translation in this regime, which inverts the methodological preference reported under misregistered binocular capture [23]. The paired Laplacian ratio (Spearman  $\rho = 0.632$  versus 0.399 for the best single-image proxy) gives a usable per-image difficulty estimator that, unlike single-image Laplacian variance, is robust to scene content.

### 5.1. Limitations

Four limitations should temper the present claims. (i) The fog-chamber capture uses flat display content rather than three-dimensional scenes, which constrains the realism of training imagery; the simulator stage and the public-haze adaptation partially, but not fully, compensate. (ii) The display, camera response, exposure, and fog radiance were not independently calibrated, so the chamber data support learned restoration but do not support radiometric inversion (Section 3). (iii) The public real-haze and NTIRE test splits are small, and the NTIRE 2026 nighttime evaluation is a two-image probe rather than a competitive ranking. (iv) The aircraft-window evaluation is reference-free; we report NIQE and demonstration videos, but PSNR/SSIM-grade evidence of cross-hardware generalization will require small aligned real-fog video sets. Radiometric calibration of the apparatus and the collection of such aligned real-fog video sets are the natural next steps.

## 6. Conclusion

We presented a controlled display-based fog imager whose exact pixel registration enables a paired fog-difficulty metric and pixel-exact reconstruction training. Pretraining on 5,495 controlled foggy/clear pairs and fine-tuning on domain-randomized synthetic fog yields a pipeline that transfers across a graded sequence of out-of-distribution settings with no target-domain training: from outdoor captures through chamber-free free-flowing fog, in which the optical depth along the line of sight is no longer fixed by a geometry, to iPhone video recorded through an aircraft cabin window in flight, directly addressing the cross-hardware transfer limitation reported for real-world binocular defogging [23]. The aircraft-window evaluation is reference-free, and a

small aligned cross-hardware test set is the natural next measurement.

Supporting evidence comes from four controlled checks. First, NAFNet leads a uniformly trained 30-model benchmark on the fog-chamber split at 24.33 dB / 0.7912 SSIM, with a compact alternative within 1.29 dB at roughly 3% of the parameter count, giving practitioners a usable accuracy–efficiency frontier. Second, a ResNet-50 classifier on foggy, defogged, and clear inputs shows that the restoration preserves semantic content rather than only low-level appearance. Third, the paired Laplacian ratio predicts per-image restoration difficulty substantially better than single-image proxies (Spearman  $\rho = 0.632$  versus 0.399), see Supplement S10. Fourth, the same backbone adapts under paired supervision to O-HAZE/NH-HAZE and to an NTIRE 2026 nighttime probe, confirming that the pipeline is not tied to the chamber distribution.

Taken together, exact registration and synthetic fine-tuning turn a laboratory fog imager into a model whose output transfers to free-flowing outdoor fog and to real aerial video without retraining. The planned release of the dataset, code, simulator, trained models, and demonstration videos is intended to catalyze further work on transferable defogging, particularly toward aligned real-fog video benchmarks that the current literature still lacks.

**Funding.** A.I. and R.M. acknowledge funding from US Department of Energy grant #55801063. S.D.M. and M.Y. acknowledges support through the Science and Engineering Apprenticeship Program (SEAP), administered by the American Society for Engineering Education (ASEE) on behalf of the Office of Naval Research, Department of the Navy. J.D.H. acknowledges support through the Naval Research Enterprise Intern Program (NREAP).

**Acknowledgment.** The support and resources from the Center for High Performance Computing at the University of Utah are gratefully acknowledged.

**Disclosures.** The authors declare no conflicts of interest. The authors used Claude (Anthropic) solely for grammar refinement and organizational suggestions.

**Data Availability.** Data and code underlying the results are available in the Supplementary Document and at <https://github.com/theMenonlab/defogging>. The fog-chamber dataset is released through Kaggle at <https://www.kaggle.com/datasets/alingold/fog-chamber>.

**Supplemental document.** See Supplement 1 for supporting content including dataset split audits, metric definitions, the full benchmark table, classification and dark-channel-prior checks, synthetic-fog tuning and fit details, public real-haze protocols, fog-density statistics, PSD analysis, and paired structure-loss analysis.

## References

1. H. Koschmieder, “Theorie der horizontalen Sichtweite,” *Beiträge zur Physik der freien Atmosphäre* **12**, 33–53 (1924).
2. S. G. Narasimhan and S. K. Nayar, “Vision and the atmosphere,” *Int. J. Comput. Vis.* **48**, 233–254 (2002).
3. K. He, J. Sun, and X. Tang, “Single image haze removal using dark channel prior,” *IEEE Trans. on Pattern Anal. Mach. Intell.* **33**, 2341–2353 (2011).
4. Q. Zhu, J. Mai, and L. Shao, “Single image dehazing using color attenuation prior,” in *British Machine Vision Conference*, (2014).
5. B. Cai, X. Xu, K. Jia, *et al.*, “DehazeNet: An end-to-end system for single image haze removal,” *IEEE Trans. on Image Process.* **25**, 5187–5198 (2016).
6. B. Li, X. Peng, Z. Wang, *et al.*, “AOD-Net: All-in-one dehazing network,” in *Proceedings of the IEEE International Conference on Computer Vision*, (2017), pp. 4770–4778.
7. X. Liu, Y. Ma, Z. Shi, and J. Chen, “GridDehazeNet: Attention-based multi-scale network for image dehazing,” in *Proceedings of the IEEE/CVF International Conference on Computer Vision*, (2019), pp. 7314–7323.
8. X. Qin, Z. Wang, Y. Bai, *et al.*, “FFA-Net: Feature fusion attention network for single image dehazing,” in *Proceedings of the AAAI Conference on Artificial Intelligence*, vol. 34 (2020), pp. 11908–11915.
9. Y. Song, Z. He, H. Qian, and X. Du, “Vision transformers for single image dehazing,” *IEEE Trans. on Image Process.* **32**, 1927–1941 (2023).
10. L. Chen, X. Chu, X. Zhang, and J. Sun, “Simple baselines for image restoration,” in *European Conference on Computer Vision*, (2022), pp. 17–33.
11. J. Gui, X. Cong, Y. Cao, *et al.*, “A comprehensive survey on image dehazing based on deep learning,” in *Proceedings of the Thirtieth International Joint Conference on Artificial Intelligence*, (2021), pp. 4426–4433.
12. G. Ros, L. Sellart, J. Materzynska, *et al.*, “The SYNTHIA dataset: A large collection of synthetic images for semantic segmentation of urban scenes,” in *Proceedings of the IEEE Conference on Computer Vision and Pattern Recognition*, (2016).

13. C. Sakaridis, D. Dai, and L. Van Gool, "Semantic foggy scene understanding with synthetic data," *Int. J. Comput. Vis.* **126**, 973–992 (2018).
14. C. Sakaridis, D. Dai, S. Hecker, and L. Van Gool, "Model adaptation with synthetic and real data for semantic dense foggy scene understanding," in *Proceedings of the European Conference on Computer Vision*, (2018), pp. 687–704.
15. P. Isola, J.-Y. Zhu, T. Zhou, and A. A. Efros, "Image-to-image translation with conditional adversarial networks," in *Proceedings of the IEEE Conference on Computer Vision and Pattern Recognition*, (2017), pp. 1125–1134.
16. J.-Y. Zhu, T. Park, P. Isola, and A. A. Efros, "Unpaired image-to-image translation using cycle-consistent adversarial networks," in *Proceedings of the IEEE International Conference on Computer Vision*, (2017), pp. 2223–2232.
17. C. O. Ancuti, C. Ancuti, C. De Vleeschouwer, and P. Bekaert, "O-HAZE: A dehazing benchmark with real hazy and haze-free outdoor images," in *Proceedings of the IEEE Conference on Computer Vision and Pattern Recognition Workshops*, (2018).
18. C. O. Ancuti, C. Ancuti, and R. Timofte, "NH-HAZE: An image dehazing benchmark with non-homogeneous hazy and haze-free images," in *Proceedings of the IEEE Conference on Computer Vision and Pattern Recognition Workshops*, (2020).
19. C. O. Ancuti, C. Ancuti, F.-A. Vasluianu, *et al.*, "NTIRE 2021 nonhomogeneous dehazing challenge report," in *Proceedings of the IEEE Conference on Computer Vision and Pattern Recognition Workshops*, (2021), pp. 627–646.
20. NTIRE 2026 Nighttime Image Dehazing Challenge organizers, "NTIRE 2026 nighttime image dehazing challenge," Codabench competition, <https://www.codabench.org/competitions/12855/> (2026). Accessed June 5, 2026.
21. Z. Chen, Z. He, Z. Lu, *et al.*, "Prompt-based test-time real image dehazing: A novel pipeline," in *Proceedings of the European Conference on Computer Vision*, (2024).
22. J. Chen, X. Yan, Q. Xu, and K. Li, "Tokenize image patches: Global context fusion for effective haze removal in large images," in *Proceedings of the IEEE/CVF Conference on Computer Vision and Pattern Recognition*, (2025), pp. 2258–2268.
23. A. Pollak and R. Menon, "Image-to-image machine translation enables computational defogging in real-world images," *Opt. Express* **32**, 33852–33860 (2024).
24. Z. Yao, S. Liu, X. Yuan, and L. Fang, "SpecAT: Spatial-spectral cumulative-attention transformer for high-resolution hyperspectral image reconstruction," in *Proceedings of the IEEE/CVF Conference on Computer Vision and Pattern Recognition (CVPR)*, (2024), pp. 25368–25377.
25. R. H. Singh, "130K images (512×512) universal image embeddings," Kaggle dataset, <https://www.kaggle.com/datasets/rhtsingh/130k-images-512x512-universal-image-embeddings> (2026). Accessed June 5, 2026.
26. D. P. Kingma and J. Ba, "Adam: A method for stochastic optimization," in *International Conference on Learning Representations (ICLR)*, (2015).
27. Z. Wang, A. C. Bovik, H. R. Sheikh, and E. P. Simoncelli, "Image quality assessment: From error visibility to structural similarity," *IEEE Trans. on Image Process.* **13**, 600–612 (2004).
28. R. Zhang, P. Isola, A. A. Efros, *et al.*, "The unreasonable effectiveness of deep features as a perceptual metric," in *Proceedings of the IEEE Conference on Computer Vision and Pattern Recognition (CVPR)*, (2018), pp. 586–595.
29. K. He, X. Zhang, S. Ren, and J. Sun, "Deep residual learning for image recognition," in *Proceedings of the IEEE Conference on Computer Vision and Pattern Recognition*, (2016), pp. 770–778.
30. G. Neuhold, T. Ollmann, S. Rota Bulò, and P. Kontschieder, "The Mapillary Vistas dataset for semantic understanding of street scenes," in *Proceedings of the IEEE International Conference on Computer Vision*, (2017), pp. 5000–5009.
31. I. Loshchilov and F. Hutter, "Decoupled weight decay regularization," in *International Conference on Learning Representations (ICLR)*, (2019).
32. R. P. Ancuti, A. Brateanu, R. Balmez, *et al.*, "Ntire 2026 nighttime image dehazing challenge report," in *Proceedings of the IEEE/CVF Conference on Computer Vision and Pattern Recognition*, (2026), pp. 1608–1625.
33. R. P. Ancuti, A. Brateanu, C. O. Ancuti, *et al.*, "Nt-haze: A benchmark dataset for realistic night-time image dehazing," in *Proceedings of the IEEE/CVF Conference on Computer Vision and Pattern Recognition*, (2026), pp. 1598–1607.
34. A. Mittal, R. Soundararajan, and A. C. Bovik, "Making a completely blind image quality analyzer," *IEEE Signal Process. Lett.* **20**, 209–212 (2013).